

A Large-Antenna Microwave Radiometer- Scatterometer Concept for Ocean and Land Sensing

E. G. Njoku¹, W. J. Wilson¹, S. H. Yueh¹, and Y. Rahmat-Samii²

¹*Jet Propulsion Laboratory
California Institute of Technology, Pasadena, CA
Tel: (818) 354-3693
Fax: (818) 354-9476
E-mail: eni.g.njoku@jpl.nasa.gov*

²*Department of Electrical Engineering
University of California, Los Angeles, CA*

Submitted for publication to:
IEEE Transactions on Geoscience and Remote Sensing

Submitted:
Revised:
Accepted:

*Jet Propulsion Laboratory
California Institute of Technology
Pasadena, CA 91109*

ABSTRACT

Microwave radiometry and scatterometry are established techniques for surface remote sensing applications. Some applications, such as measurement of sea surface salinity, sea surface temperature, and soil moisture, require low frequency observations (~ 6 GHz and below) and sensors with large antennas to achieve adequate spatial resolution. Potential benefits can be obtained by observing simultaneously with passive and active channels, at similar frequencies, viewing angles, and spatial resolutions, making use of the complementary information contained in the emissivity and backscattering signatures of land and ocean targets. In this study we investigate a concept for combined passive and active multichannel sensing, with high spatial resolution, high measurement sensitivity and calibration accuracy, and wide swath for frequent global coverage. The system consists of a lightweight, rotating, mesh deployable antenna with offset feeds. Our analysis focuses on the measurement of sea surface salinity since this application drives the system requirements and is a high science priority for which no spaceborne capability exists. Demonstration of a capability for sea surface salinity enhances the potential of this concept for other applications, including high-resolution measurements of soil moisture, ocean winds, precipitation, sea-surface temperature, and sea-ice.

I. INTRODUCTION

Remote sensing of sea surface salinity (SSS), sea surface temperature (SST), and soil moisture requires frequencies in the 1–6 GHz range for adequate sensitivity to the parameters of interest. At these frequencies, antennas with aperture diameters of ~ 6 m or greater are needed to obtain spatial resolutions of ~ 30 km or better from low Earth orbit. Earlier [1] we studied an inflatable antenna concept as a means for achieving a large aperture, with low mass, for spaceborne passive sensing at L and S bands. Demonstrations of inflatable antenna systems in space during the next 5–10 years should reduce significantly the risk of this technology for a future remote sensing mission. In this paper, we have studied a concept for combined passive and active (real-aperture) sensing at 1–6 GHz, using a 6- to 10-m-diameter, low-mass, deployable mesh antenna. The antenna system consists of a rotating, offset-fed parabolic reflector, with a cluster of multichannel feedhorns shared by radiometer and radar subsystems in one sensor package. The system measures microwave emission and backscatter from the Earth's surface, effectively simultaneously at multiple frequencies and polarizations. The key technology in this system is the lightweight mesh antenna. The reflector surface is a tensioned gold-plated molybdenum wire-mesh, supported by a rigid rib or truss structure which can be folded compactly for launch and deployed on orbit. Large antennas of this construction, at sizes up to ~ 12 m, have been developed

and space-qualified in the commercial sector, and are planned for launch on geostationary communication satellites starting in 1999 [2]. Their use for remote sensing applications requires careful study due to the unique requirements for radiometric precision and accuracy, and the demands on spacecraft attitude control imposed by a large rotating antenna system.

The rationale for considering a combined passive and active sensor is that complementary information contained in the surface emissivity and backscattering signatures can provide enhanced retrieval accuracy of geophysical parameters. Over ocean, passive (radiometric) measurements provide the primary information for estimating SSS and SST. Active (scatterometer) measurements are a primary source of information on wind-induced surface roughness, providing corrections to the radiometric measurements. Over land, radiometric measurements provide the primary information for estimating soil moisture, while scatterometer measurements can provide corrections for surface roughness and vegetation. The simulations described in Section V indicate that a 6-m antenna radiometer-scatterometer system should be capable of providing SSS estimates with an accuracy of ~ 0.2 psu at 100-km spatial resolution. Previous simulations [1] have shown that soil moisture estimates of accuracy ~ 0.04 g cm⁻³ at 40-km spatial resolution should be obtainable.

A key feature of the antenna concept studied here is the potential for extending the frequency range and number of channels by increasing the number of feedhorns (or feedhorn ports) at the reflector focus to accommodate the additional channels. This broadens the applications of this concept to include measurements of ocean wind speed, wind direction, precipitation, sea-ice, snow, and other environmental parameters in addition to SSS, SST, and soil moisture. With a large antenna, these measurements can be made at much higher spatial resolutions than are currently feasible. Table 1 shows the heritage of spaceborne passive microwave surface-sensing instruments. The mesh antenna concept is a logical extension of this heritage to larger-aperture systems, and provides a capability for new measurements and higher spatial resolutions, while keeping the sensor cost low.

The antenna configuration described here is not unique, and has not been optimized for a particular spacecraft platform. Alternate configurations for mesh antennas such as a parabolic-torus reflector with scanning or pushbroom feeds can also be considered, and are currently being investigated. Parabolic torus designs have merit in that they do not require a rotating reflector. However, the required reflector diameter is much larger. The choice of a particular spacecraft platform depends on whether a dedicated or shared mission is being considered, and on other power, mass, and accommodations constraints.

II. MEASUREMENT REQUIREMENTS

A. *Science Objectives*

The principles and challenges of satellite SSS remote sensing at microwave frequencies have been recognized for over two decades [3], [4]. Three primary scientific objectives for SSS sensing have been described [5]. These objectives are: (1) improving seasonal-to-interannual El Nino Southern Oscillation (ENSO) climate predictions; (2) improving ocean rainfall estimates and global hydrologic budgets; and (3) monitoring large-scale salinity events, such as tracking interannual SSS variability in the Nordic Seas. Specific accuracy requirements for these objectives vary with the space and time scales of the phenomena to be resolved [5]. The signal for the ENSO problem is estimated to have a length scale of >100 km, a weekly time scale, and a strength of $0.05\text{--}1$ psu. The accuracy requirement for the surface water flux problem has been estimated as ~ 0.05 psu, at $2^\circ \times 2^\circ$ lat-lon and monthly resolution in low to mid latitudes, while the high-latitude salinity variability signal is ~ 0.01 psu at ~ 100 km. This latter signal will be extremely difficult to detect using remote sensing. To address the first two objectives we have adopted a design accuracy target of 0.2 psu, at 100-km and weekly space and time scales. As discussed in Section V, depending on the correlation scales of the measurement errors and the ability to assimilate in situ data for calibration, improved accuracy may be achievable at larger space and time scales.

B. *Modeling*

At frequencies below ~ 3 GHz, changes in SSS cause significant changes in the sea water dielectric constant, thus changing the surface emissivity and the emitted brightness temperature [6]. SSS can thus be inferred from observations of ocean brightness temperature in this frequency range. Other geophysical factors also affect the observed brightness temperatures, such as SST, wind-induced roughness, atmospheric attenuation, sun glint, Faraday rotation, and galactic noise. Correction or avoidance of these factors is therefore necessary to estimate SSS accurately. Figure 1 shows the computed dependence of brightness temperature on frequency in the range $1\text{--}20$ GHz, at 50° incidence angle, for vertical and horizontal polarizations. The curves were computed using an ocean surface emission model based on the work of Hollinger [7], Stogryn [8], and Klein and Swift [9], and an atmospheric layer to include the effects of precipitable water. The baseline parameter values used were: T_s (SST) = 25 C, S (SSS) = 35 psu, v (wind speed) = 10 m s $^{-1}$, q_v (precipitable water) = 3.0 g cm $^{-2}$, and θ (incidence angle) = 50° . The decrease in brightness temperature below ~ 3 GHz is due to the effect of salinity, while the increasing brightness temperature above ~ 15 GHz is due to the 22 GHz atmospheric water vapor absorption line.

Figures 2(a) and (b) show the computed sensitivities of brightness temperature T_B to SST, SSS, and wind speed, as functions of frequency, for vertical and horizontal polarizations respectively. The sensitivity is defined as $\partial T_B / \partial p$, where p is one of the parameters T_s , S , or v . The same baseline parameters were used in computing Figure 2 as in Figure 1. The effects of geophysical parameter variations on brightness temperature are nonlinear, such that the sensitivities depend on the parameter values at which they are computed. For example the magnitude of the sensitivity to SSS at 1.4 GHz and vertical polarization decreases from 0.77 K/psu (as shown in Figure 2(a)) to 0.57 K/psu for a decrease in SST from 25 to 15 C. (Note that the scale for sensitivity to SSS is negative). However, the frequency and polarization dependences shown in Figures 2(a) and (b) are representative of the typical range of parameter values. The magnitude of the sensitivity to SSS decreases rapidly as frequency increases. The sensitivity to SST increases from a negative value to a peak in the broad range of 4–10 GHz. The sensitivity to wind speed increases with frequency until atmospheric effects reduce the sensitivity above ~17 GHz. The sensitivities to SSS and SST are greater at V than at H polarization, while the converse is true for wind speed.

C. Retrieval

The differences in sensitivity to T_s , S , and v as functions of frequency and polarization allow these parameters to be estimated independently using multifrequency, dual-polarization measurements. L band is the optimum frequency range for sensing SSS, since the brightness temperature sensitivity to SSS is high, and the sensitivities to SST and wind speed are low, in this range. Dual-polarized measurements at S or C bands have higher sensitivities to SST and wind speed than at L band, and lower sensitivities to SSS, and hence can be used to correct for the effects of SST and wind speed in estimation of SSS. To provide additional sensitivity and accuracy for the wind-induced roughness correction it is desirable that scatterometer (radar backscatter) measurements at L band be included. Radar backscatter is more sensitive to surface roughness than radiometric emissivity, and is relatively insensitive to SSS and SST. It is also desirable that the radar and radiometer measurements be made at approximately the same frequency and spatial resolution so that similar roughness and spatial scales are sensed.

In this study we have considered an integrated radiometer-scatterometer system that includes radiometers operating at 1.41 (L band) and 2.69 GHz (C band) with V and H polarizations, and a scatterometer operating at 1.26 GHz (L band) with VV and HH polarizations. The system characteristics are described in Section III. The frequencies at L and S bands were chosen to fit within the spectrum allocations for passive and active remote sensing services [10]. We have not attempted to optimize the selection of measurement channels by minimizing for example the SSS

retrieval error as a function of different multichannel combinations. However, the simulations in Section V indicate the benefits of including the radar channels in addition to radiometric channels alone. It is straightforward to add or substitute a frequency at ~ 6 GHz if subsequent simulations or experimental measurements show that this provides improved SSS retrieval performance. The two key issues addressed in the following sections are: (1) determining via simulations how well SSS can be measured using the baseline multichannel passive/active sensor described in Section III; and (2) determining the performance specifications required of the sensor for such SSS measurements.

III. SYSTEM CONCEPT

A. Reflector

The surface mesh of the antenna reflector is fabricated from gold-plated molybdenum wire, typically of ~ 1.2 -mil diameter, knit into a diamond shaped pattern. A 10-opening-per-inch knit density is common, which provides excellent reflectivity up to X-band and above. The loose nature of the knit allows the individual wires to shift relative to each other when not under tension. This characteristic allows the mesh to be stowed compactly and then stretched to the deployed configuration with minimal short wavelength surface error. The reflectivity and transmission loss characteristics of these wire meshes have been studied by many investigators, e.g. [11], [12]. The surface shaping mechanism is a tensioned cable or web network that provides a tie-down structure for the large number of flexible ties that interface to the mesh reflector. The larger the number of ties, the higher the surface precision. Various designs have been developed for the outer rigid support structure. Two designs of current interest are the “radial rib” and the “perimeter truss”. The perimeter truss is a relatively new concept, based on a toroidal-shaped structure that supports the mesh and its surface-shaping network of geodesic nets and ties at their outer perimeter [13]. The truss structure stows compactly forming a hollow cylinder containing the nets, mesh, and ties. The mass of the 6-m reflector (excluding deployment boom and feeds) is less than ~ 15 kg. The RSS (root-sum-squared) error for the 6-m reflector surface, accounting for all sources, is less than 0.6 mm. This gives a $\lambda / 20$ or better surface precision performance at frequencies up to 25 GHz (where λ is the wavelength). Mesh deployable antennas in the 12-m-diameter size range, of both radial rib and perimeter truss designs, are planned to be launched in 1999 and 2000 for geostationary communication satellite applications [2]. These commercial-sector launches, and their follow-ons, will demonstrate the deployment reliability and performance in space of these new types of antennas.

B. System Characteristics

A schematic of the 6-m antenna concept is shown in Figure 3, and its characteristics are given in Table 2. The antenna is a rotating, offset-fed, parabolic mesh reflector, with a cluster of three feedhorns. The combined antenna and feed system rotates about a vertical axis with antenna beams offset at a constant angle from nadir, providing a conical scan and wide swath. As the spacecraft moves, the 3-dB antenna footprints provide overlap along and across track. In addition to the 6-m antenna shown, a configuration using a 10-m antenna has also been studied which would provide higher spatial resolution. However, the 6-m diameter is a compromise that provides adequate spatial resolution for the science objectives while being a feasible first step for a spaceborne remote sensing mission. The antenna is shown deployed below a small spacecraft that rotates with the antenna. Also being studied is a configuration using a non-rotating, three-axis-stabilized platform, with the antenna mounted either above or below the spacecraft.

Each of the three feedhorns serves all the 1.41 and 2.69 GHz passive and 1.26 GHz active channels. The three feedhorns provide three separate beams, allowing the reflector to rotate at the relatively moderate rate of 6.6 rpm. Under-illumination of the main reflector at 2.69 GHz provides roughly equal beamwidths at 1.41 and 2.69 GHz. The radiometer integration times and antenna rotation rate of 6.6 rpm provide Nyquist sampling, with sample spacing at half the 3-dB footprint dimension. The use of three feedhorns allows the antenna to rotate at one-third the rate required with a single feedhorn for the same footprint overlap. The trade-off between reduced spin-rate and increased mass at the reflector focus must be studied as a function of the impact on the spacecraft attitude control system. The footprint sampling pattern shown in Figure 3 is schematic only, and not to scale. The forward portion (180° of the total 360°) of the actual footprint pattern is shown to scale in Figure 4. In practice, the fore and aft views of the surface can be used to investigate the azimuthal dependence of ocean surface emission at 1–3 GHz due to wind speed. This dependence may be negligible or small, in which case the two views of a given surface location can be averaged to improve the measurement sensitivity by a factor of up to 1.4.

C. Spacecraft Requirements

This study addresses primarily the antenna configuration and not the spacecraft and attitude control system (ACS). A preliminary industry study has shown, however, that the system pointing and control requirements can be met using standard “off-the-shelf” spacecraft and ACS momentum compensation components. The integrated spacecraft-sensor system can be packaged for launch in a Taurus-class launch vehicle.

IV. FEED/REFLECTOR CONFIGURATION

The combined feed and reflector configuration is designed to optimize trade-offs between compactness, antenna beam performance, footprint sampling pattern, and reflector spin rate. Parameters of the feed/reflector configuration include focal length, tilt angle (angle between the antenna rotation axis and boresight), feed dimensions, placements, beamwidths, and cross-polarization levels. Antenna patterns have been computed for the optimized configuration to verify its performance characteristics. Results are shown here for the 10-m-diameter antenna. Results for the 6-m antenna scale straightforwardly from the 10-m results. Figures 5 and 6 show the reflector and conical feedhorn geometries and dimensions. The feedhorns are symmetric, and only one half of the section is shown. Figures 7 (a) and 7 (b) show the L and S-band far-field antenna patterns for one of the three beams. The other two beams have similar patterns. The feedhorns are designed to under-illuminate the reflector at 2.69 GHz to provide roughly equal beamwidths at 1.41 and 2.69 GHz. This improves the multifrequency retrieval accuracy since the same scene dimensions are being viewed at both frequencies. Table 3 shows the computed antenna pattern characteristics, including beamwidths and beam efficiencies, for both ideal and conical-horn feeds, and for at-focus and off-focus positions. From these results it is clear that the antenna design provides more than adequate beam performance for the remote sensing applications.

V. ERROR ANALYSIS

A. *Simulations*

Retrieval simulations have been performed for SSS (and earlier for soil moisture [1]) to verify that the system design meets the science accuracy requirements as influenced by anticipated instrument-related error sources and geophysical noise. The simulations have been performed in greater detail for SSS since this parameter places more stringent requirements on the system design. The SSS error analysis is based on a performance simulation tool which simulates L and S band radiometer and radar measurements for given satellite orbit characteristics, instrument design, and system performance, including antenna rotation rate, antenna beam pointing accuracy, and spacecraft attitude errors. Measurement errors include geophysical modeling noise, radiometer and radar signal detection sensitivities, and sensor calibration errors. Using climatologies of SSS and SST, wind speeds from the ECMWF (European Centre for Medium-range Weather Forecasting) analyses, and SSM/I (Special Sensor Microwave/Imager) monthly-averaged atmospheric water vapor and cloud liquid water paths as input fields, a set of radiometer and radar simulated measurement data was computed for incidence angles of 40° and 45°. The simulated noisy sensor data were processed using a conjugate-gradient method to retrieve SSS and SST by minimizing a

normalized least-square measure. The results were averaged over a 7-day (weekly) period on a $1^\circ \times 1^\circ$ lat-lon grid (~ 100 km spatial resolution) for one set of input fields for the month of May.

Table 4 shows the assumptions used for the simulated errors. The errors consist of three terms including the noise equivalent delta-T (ΔT_n), the geophysical modeling error (ΔT_m), and the calibration error (ΔT_r). The radiometer design under consideration is a total power radiometer with ΔT_n determined by the system noise temperature normalized by the square root of the time and bandwidth product. The geophysical modeling error ΔT_m includes errors in modeling the effects of sea surface roughness, atmospheric attenuation, and the ionosphere. ΔT_r represents the time-varying portion of the system calibration errors. All the error terms are assumed to be Gaussian with zero mean. Constant calibration bias offsets are assumed to be removable by adjustment to in-situ calibration data. To account for the time-varying characteristics of the calibration errors, ΔT_r is modeled as a first-order Markov random process with a correlation time τ . If we assume a nominal orbit altitude of 600 km, the spacecraft will travel by about 1600 km in 4 minutes. Thus, for a correlation time of four minutes or greater, the fore- and aft-look measurements of any pixel within the swath will be correlated. For our analysis, we have assumed a correlation time of 4 minutes for ΔT_r . Should a smaller correlation time be assumed such that the fore- and aft-look calibration errors are uncorrelated, the contribution of these errors will be reduced by averaging the two independent estimates. ΔT_m is treated as a spatial random process with a correlation length of 50 km. The magnitudes of the simulated errors are summarized in Table 4 for data averaged within 50-km and 100-km square bins.

The weekly-averaged retrieval results are shown in Figure 8 as a set of color maps showing the global distributions of SSS and SST. The figure shows the input fields (“true” fields), the retrieved fields, and the differences between the fields, for a 40° incidence angle. (The errors are similar at 40° and 45° incidence angles.) Comparing the retrieved fields with the true fields, it is seen that the main features of the SSS and SST fields are correctly retrieved. The difference (“delta”) maps exhibit vertical striations which reflect the effects of the time-correlated calibration errors in the data (which consist of many relatively narrow swaths).

The SSS RMS retrieval errors are shown in Figure 9, for 20° latitude bands at a 40° incidence angle. At higher latitudes the retrieval errors are greater because the sensitivity to SSS decreases as SST decreases. Including the L-band radar in the retrieval reduces the RMS error by 0.05–0.1

psu. The improvement comes from the enhanced correction for surface roughness. The improved accuracy and extra capabilities contributed by the radar must, however, be traded against the increased cost of the system. The results of these simulations show that for 100 km spatial resolution and 1-week averaging the salinity measurements are expected to have errors of <0.15 psu in the tropics and sub-tropics and <0.3 psu in sub-polar regions. It is expected that additional accuracy can be realized with further space-time averaging, and by co-analysis with in-situ surface data, to resolve weaker signals on longer time scales. This suggests that this instrument concept can meet the target measurement requirements (Section II), assuming that the assumptions for instrument noise and calibration errors of Table 4 are reasonable. Thus, we find that to achieve the required accuracy for SSS, a radiometer with rms noise (ΔT) of 0.1 K per pixel and calibration stability of 0.2 K is adequate. In addition, a radar backscatter calibration stability of ~ 0.2 dB is required. These requirements have been derived for an incidence angle in the range of $40\text{--}45^\circ$. It is assumed that bias effects on the geophysical retrievals due to absolute accuracies of ~ 1 K and ~ 1 dB for the radiometer and radar, respectively, can be removed by post-launch adjustments to in situ calibration references.

Also shown in Figure 9 are the simulated RMS errors for an L/S-band cross-track-scanning radiometer. Only the two outer 300–600 km portions of the swath (corresponding to approximately $25\text{--}45^\circ$ from nadir) were used in the simulations. This is because closer to nadir the difference between horizontal and vertical polarized emission decreases, and the polarization difference provides less information for correcting surface roughness. Even by restricting the swath to these angles, the retrieval error is significantly degraded over the conical-scan case. This indicates the significant benefit of the conical-scan configuration for salinity sensing.

A simulation was also performed to determine the sensitivity of the retrievals to characteristics of the sensor calibration errors. This simulation assumed a calibration error correlation time of eight seconds as compared with the earlier assumed correlation time of four minutes. The shorter correlation time resulted in a significant reduction of artifacts in retrieved SSS anomalies in the north and equatorial Pacific due to the increased number of independent samples. This suggests that a frequent calibration (every few seconds) is desirable for a microwave salinity sensor to reduce the effects of time varying calibration bias.

B. Calibration Error Budget

To assess how well the assumed calibration accuracies can be realized, a calibration budget is shown in Table 5. It is assumed that the absolute calibration bias can be corrected by empirical comparisons of radiometer and radar observations with in-situ data through adjustment of the

geophysical model functions. The geophysical retrieval performance is then limited by the temporal stability of the calibration. Errors due to non-ideal antenna patterns can be limited to less than 0.1 K for beam efficiencies of greater than 90%. The mesh reflector shaping and support structures are constructed of composite and temperature-insensitive materials that are thermally stable in orbit. In addition, the mesh surface shape can be monitored by optical techniques such as developed for the Shuttle Radar Topography Mission (SRTM). An antenna beam-pointing error of 0.1° should be feasible. The accuracy of 0.01° for spacecraft attitude can be achieved by using star trackers. The stability of the noise source for radiometer calibration has been demonstrated for the JASON (TOPEX follow-on) microwave radiometers. The stability of the radar calibration loop has been demonstrated by system and integration testing of the SeaWinds scatterometer (follow-on to NSCAT). The effects of the small losses in the antenna reflector and feed horns can be corrected by careful temperature measurements of these components. In summary, the RSS calibration stability requirements of 0.2 K and 0.19 dB for the radiometers and radar, respectively, appear challenging but feasible.

VI. GEOPHYSICAL ERROR SOURCES

The geophysical modeling error of $\Delta T_m = 0.2$ K assumed in Table 4 is also a challenging target. As this is a requirement on relative and not absolute error, it is related to the error in modeling geophysical variability. To estimate the feasibility of this target for salinity sensing we must consider the contributing geophysical error sources and their impact on the retrievals. Table 6 lists the major geophysical variability effects on the relationship between brightness temperature and SSS at L-band. The symbols indicate which effects can potentially be corrected in retrieving SSS. For comparison, the effects on retrieving soil moisture are also listed. Where effects that cannot be corrected contaminate the data, the data must be identified (flagged) and rejected. "Minor" correctable effects are those that influence the brightness temperature by less than a few Kelvins and can be modeled and removed accurately using climatological knowledge. "Major" correctable effects require either multichannel information or ancillary data from other sources to implement a correction in the retrieval algorithm.

Rain, solar radiation (either entering the antenna sidelobes directly or reflected off the ocean surface), radio-frequency interference (RFI), and galactic-center emission have large L-band brightness temperature signatures which cannot be modeled or measured accurately enough for correction. The presence of these interferences can be detected (or inferred from geometrical considerations in the case of solar and galactic radiation) so that the contaminated data can be rejected from the data stream. Only a small fraction of the data should require rejection due to these

causes. RFI is likely to cause the most data rejection over land, while reflected solar radiation will likely be the cause for most data rejection over ocean. The effects of atmospheric water vapor and clouds on brightness temperature at L band are small, and can be estimated from climatology. The residual uncertainty in brightness temperature due to these effects is estimated as less than 0.1 K.

Uncertainties in the surface emissivity model affect the accuracy with which surface temperature and surface roughness effects can be corrected. However, for the ocean surface at L band the effects of wind-induced roughness and foam are small. In the multi-polarization L-band (passive and active) retrieval approach, where the appropriate roughness scale is being directly sensed and corrected, an uncertainty of 0.15 K is considered reasonable. This uncertainty is expected to be significantly larger if ancillary data on wind speed has to be used instead of a multichannel correction, since the relationship between wind speed and L-band surface roughness is indirect and may introduce additional error.

The effects of Faraday rotation have been modeled for the orbit and scan configuration described here [14]. A pre-dawn equator crossing and sun-synchronous orbit are desirable to minimize the ionospheric effects. By using the sum of the vertically and horizontally polarized channels (which is insensitive to Faraday rotation) or by providing an additional polarimetric channel in the radiometers, it should be possible to reduce the uncertainty due to Faraday rotation to less than 0.1 K. Combining the effects of uncertainties due to atmospheric variability, surface emissivity, and Faraday rotation, the RSS target of $\Delta T_m = 0.2$ K appears achievable.

VII. DISCUSSION

In this paper a system configuration has been studied for a multichannel (passive and active) microwave spaceborne sensor operating in the 1–6 GHz range, using a large-aperture (6–10 m) low-mass, rotating, offset-fed parabolic antenna. Simulations have shown that the system should be capable of meeting the spatial and temporal resolution and accuracy requirements of sea surface salinity sensing. For the configuration studied, the instrument specifications have been shown to meet the science requirements. These specifications are all within the current technology state of the art. However, very careful design of the RF, mechanical, and calibration systems will be required to meet the performance goals.

Recommendations for future work include further studies of: (1) radiometric performance of reflector mesh materials, including mesh thermal emission under variable heating and thermal gradients, to verify that solar illumination effects on calibration stability in orbit are minimal; (2) system rotational dynamics, including reflector, boom, and feeds, under simulated spaceborne

conditions, to verify that the attitude control and beam pointing tolerances can be maintained; and (3) optimal channel selections, and mitigation of Faraday rotation effects through use of polarimetric channels. These studies are presently being carried out at JPL under NASA's Instrument Incubator Program. In addition, a dual-polarized L and S band integrated radar/radiometer aircraft instrument has been built to validate the improved capability of passive/active multichannel sensing for precision ocean salinity and soil moisture measurement through field experiments. The aircraft instrument uses two dual-polarized conical horn antennas with adjustable incidence angle (non-scanning). The radiometric sensitivity is designed to be better than 0.1 K per pixel, with an anticipated accuracy stability of ~ 0.1 K. The first flights of this instrument are scheduled for early 1999.

ACKNOWLEDGMENT

This work represents one phase of research carried out at the Jet Propulsion Laboratory, California Institute of Technology, under contract with the National Aeronautics and Space Administration.

REFERENCES

- [1] E. G. Njoku, Y. Rahmat-Samii, J. Sercel, W. Wilson, and M. Moghaddam, "Evaluation of an inflatable antenna concept for microwave sensing of soil moisture and ocean salinity," *IEEE Trans. Geosci. Remote Sens.*, (January issue), 1999.
- [2] B. Miller, "Satellites free the mobile phone," *IEEE Spectrum*, vol. 35, pp. 26-35, 1998.
- [3] C. T. Swift and R. McIntosh, "Consideration for microwave remote sensing of ocean surface salinity," *IEEE Trans. Geosci. Remote Sens.*, vol. GE-21, pp. 480-491, 1983.
- [4] G. S. Lagerloef, C. T. Swift, and D. M. LeVine, "Sea surface salinity: The next remote sensing challenge," *Oceanography*, vol. 8, pp. 44-50, 1995.
- [5] G. S. Lagerloef (Ed.), "Report of the first workshop, Salinity Sea Ice Working Group (SSIWG), La Jolla, CA, 7-8 February 1998," <http://www.esr.org>, Earth and Space Research, Seattle, WA, 1998.
- [6] C. T. Swift, "Passive microwave remote sensing of the ocean - A review," *Boundary-Layer Meteorol.*, vol. 18, pp. 25-54, 1980.
- [7] J. P. Hollinger "Passive microwave measurements of sea surface roughness," *IEEE Trans. Geosci. Electr.*, vol. GE-9, pp. 165-169, 1971.

- [8] A. Stogryn, "The emissivity of sea foam at microwave frequencies," *J. Geophys. Res.*, vol. 77, pp. 1658-1666, 1972.
- [9] L. A. Klein and C. T. Swift, "An improved model for the dielectric constant of sea water," *IEEE Trans. Antennas. and Propagat.*, vol. AP-25, pp. 104-111, 1977.
- [10] V. Litman and J. Nicholas, "Guidelines for spaceborne microwave remote sensors," *NASA Reference Publication RP-1086*, National Aeronautics and Space Administration, Washington, DC, 1982.
- [11] Y. Rahmat-Samii and S. W. Lee, "Vector diffraction analysis of reflector antennas with mesh surfaces," *IEEE Trans. Antennas. and Propagat.*, vol. AP-33, pp. 76-90, 1985.
- [12] W. Imbriale, V. Galindo-Israel, and Y. Rahmat-Samii, "On the reflectivity of complex mesh surfaces," *IEEE Trans. Antennas. and Propagat.*, vol. AP-39, pp. 1352-1365, 1991.
- [13] M. W. Thomson, "The AstroMesh deployable reflector," *Symposium on Deployable Structures: Theory and Applications*, International Union of Applied and Theoretical Mechanics, and International Assoc. of Shell and Spatial Structures, Cambridge, U.K., 6-9 September, 1998.
- [14] Njoku, E. G. and M. Moghaddam, "Effects of ionospheric variability on passive sensing of the Earth at 1-3 GHz," *Radio Science* (*submitted*).

Table 1: Heritage and characteristics of passive microwave Earth-imaging sensors (SMMR, SSM/I, and AMSR), compared with the large-aperture mesh antenna concept.

Parameter	SMMR (Nimbus-7)	SSM/I (DMSP)	AMSR* (ADEOS-II/EOS)	Mesh Antenna Concept [†]
Frequencies (GHz)	6.6, 10.7, 18, 21, 37	19.3, 22.3, 37, 85.5	6.9, 10.7, 18.7, 23.8, 36.5, 89	1.4, 2.7, (6.9), (10.7), (19)
Altitude (km)	955	860	705	600–800
Antenna size (m)	0.8	0.6	1.6	6–10
Incidence angle (deg)	50.3	53.1	55	40–55
Footprint size (km)				
at ~ 7 GHz	140	n/a	65	<15
at ~19 GHz	55	68	23	(<6)
Swath width (km)	780	1400	1445	~1200
Launch date	1978	1987—Series	2000	

* EOS values are shown.

[†] Only 1.4 and 2.7 GHz frequencies are considered here. However the mesh antenna provides good performance at frequencies up to >19 GHz. Ranges and approximate values are shown, subject to system trade-offs.

Table 2: System characteristics

Radiometer Frequencies	1.41 and 2.69 GHz
Polarization	V and H
Radar Frequency	1.26 GHz
Radar Polarization Modes	VV, HH
Antenna Aperture	6 m
Antenna Beamwidth	2.4°
Antenna Beam Efficiency	> 90%
Orbit altitude	600 km
Incidence Angle	40°
Footprint Size	35 x 45 km
Swath Width	900 km
No. Antenna Beams per frequency	3
Rotation Rate	6.6 rpm
RMS Noise per pixel (B = 100 MHz)*	0.1 K
Radiometer Calibration Stability	< 0.2 K
Radiometer Absolute Calibration Accuracy	1.0 K
Radar Calibration Stability (1 σ)	0.2 dB
Radar Calibration Accuracy	1 dB
Radar Transmit Power and Duty Cycle	200 Watts and 10%
Data Rate	12 Kbits/sec or 120 Mbytes/day
Power	300 Watts
Radiometers and Feeds Mass	12 kg
Antenna Mass	~ 15 kg

* Over ocean, and averaging forward and rear pixels. Over land, the bandwidths are reduced to 25 MHz and 10 MHz at 1.41 and 2.69 GHz, respectively, to minimize radio-frequency interference.

Table 3: Antenna pattern characteristics (10-m diameter)

SMRM	L-Band				S-Band			
	D [dB]	AE [%]	BW [°]	BE [%]	D [dB]	AE [%]	BW [°]	BE [%]
IH, A-F	42.05	73.59	1.38	95.21	46.16	52.08	1.52	99.85
CH, A-F	41.39	63.20	1.56	90.42	38.62	9.16	1.72	96.40
IH, O-F	41.95	71.88	1.53	95.37	45.76	47.46	1.68	99.87
CH, O-F	41.43	63.79	1.56	89.96	39.47	11.16	1.92	96.51

D = Directivity

AE = Antenna Efficiency

BW = BeamWidth

BE = Beam Efficiency

IH = Ideal horn feed model CH = Conical Horn Feed

A-F = At Focus

O-F = Off Focus ($\Delta x = 0.25$ m, $BT = 1.8^\circ$)

Table 4: Error characteristics assumed in the SSS retrieval simulations. ΔT_n = instrument noise, ΔT_m = modeling error, ΔT_r = calibration error (time-varying). Cases for two spatial resolutions, 50 and 100 km, are shown.

Spatial Resolution	ΔT_n (K)	ΔT_m (K)	ΔT_r (K)	RSS ΔT (K)
50 km	0.07	0.2	0.2	0.29
100 km	0.035	0.1	0.2	0.23

Table 5: Calibration requirements summary

	Stability (1 sigma)			Bias (3 sigma)		
Parameter	Parameter Error	Radiometer (K)	Radar (dB)	Parameter Error	Radiometer (K)	Radar (dB)
Antenna Beam Gain and Pattern		0.1	0.15		2	0.7
Antenna Beam Pointing	0.1°	0.15	0.1	0.3°	0.45	0.3
S/C Attitude	0.01°	0.02	0.01	0.03°	0.05	0.03
Calibration Noise Source	0.1 K	0.1	0	1 K	1	0
Radar Calibration Loop	0.05 dB	0	0.05	1	0	1
Waveguide/ Coax cable loss	0.05 dB	0.05	0.01	0.1 dB	0.1	0.1
RSS		0.2	0.19		2.5	0.9

Table 6: Geophysical effects on the relationship between brightness temperature and sea surface salinity and soil moisture

Effect	Salinity	Soil Moisture
Rain	x	x
Solar radiation	x	x
Radio-frequency interference	x	x
Galactic emission	x	+
Atmospheric gases	+	
Clouds	+	
Faraday rotation	o	o
Surface temperature	o	o
Surface roughness	o	o
Vegetation		o
Soil texture		+

x Major effect, uncorrectable. Flag and reject.

+ Minor effect, correctable using climatology.

o Major effect, correctable using multichannel retrieval or ancillary data.

FIGURE CAPTIONS

- Figure 1: Dependence of brightness temperature on frequency at 50° incidence angle for vertical (V) and horizontal (H) polarizations, and for $T_s = 25$ C, $S = 35$ psu, $v = 10$ m s⁻¹, $q_v = 3.0$ g cm⁻² and no cloud.
- Figure 2: Brightness temperature sensitivities to SST, SSS, and wind speed as functions of frequency, for (a) vertical and (b) horizontal polarizations. A separate scale is provided for each curve. (For SSS the curves have been displayed with negative units.) The baseline parameters used in the computations are the same as in Figure 1.
- Figure 3: Schematic of the large-aperture mesh antenna concept. (The footprint sampling pattern is not to scale.)
- Figure 4: Segment of footprint sampling pattern shown to scale with latitude-longitude markings.
- Figure 5: Schematic cross-section of the antenna reflector showing the geometry and optimized dimensions (10-m-diameter antenna shown). Aperture diameter $D = 10$ m, focal length $F = 6$ m, and tilt angle $\alpha = 47.27^\circ$. The rotation axis is in the direction Z_f (zenith direction).
- Figure 6: Conical feedhorn geometry and dimensions. Since the feedhorn is symmetric only one half of the cross-section is shown. $R = 0.21$ m, $L = 0.67$ m, $R_0 = 0.075$ m.
- Figure 7: Far-field antenna patterns for the 10-m parabolic reflector: (a) L band; (b) S band.
- Figure 8: Simulated 7-day global retrievals of SSS and SST using realistic orbit and instrument sampling, and assuming combined L/S-band-radiometer and L-band-radar measurements. “True” SSS and SST are input climatological fields. “Delta” SSS and SST are the differences between true and retrieved fields.
- Figure 9: Simulated salinity RMS retrieval errors (7 days of data) in 20° latitude bins. Separate simulations were performed for a conical-scan L/S-band radiometer, a conical-scan L/S-band radiometer and L-band radar combined, and a cross-track-scanning L/S-band radiometer.

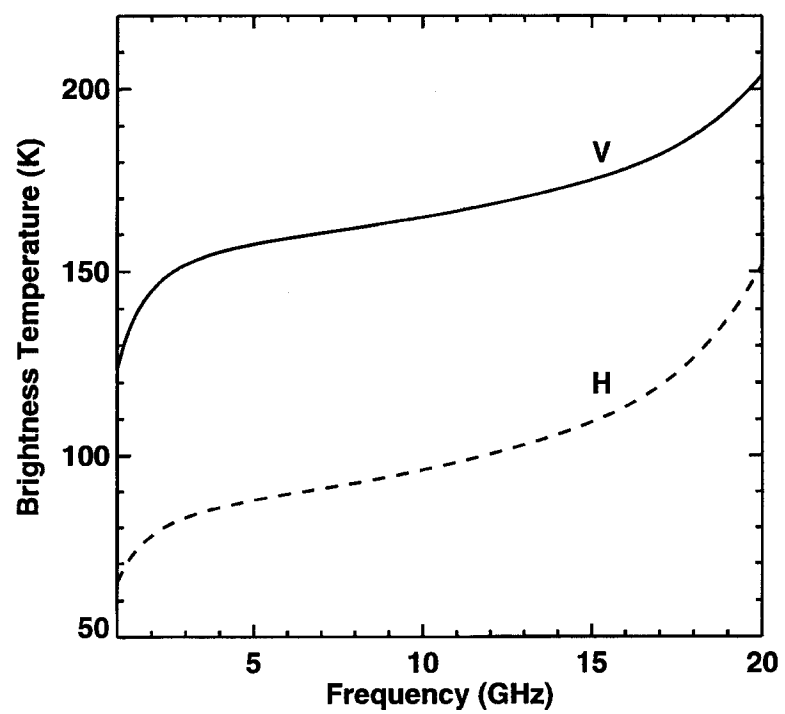


Figure 1

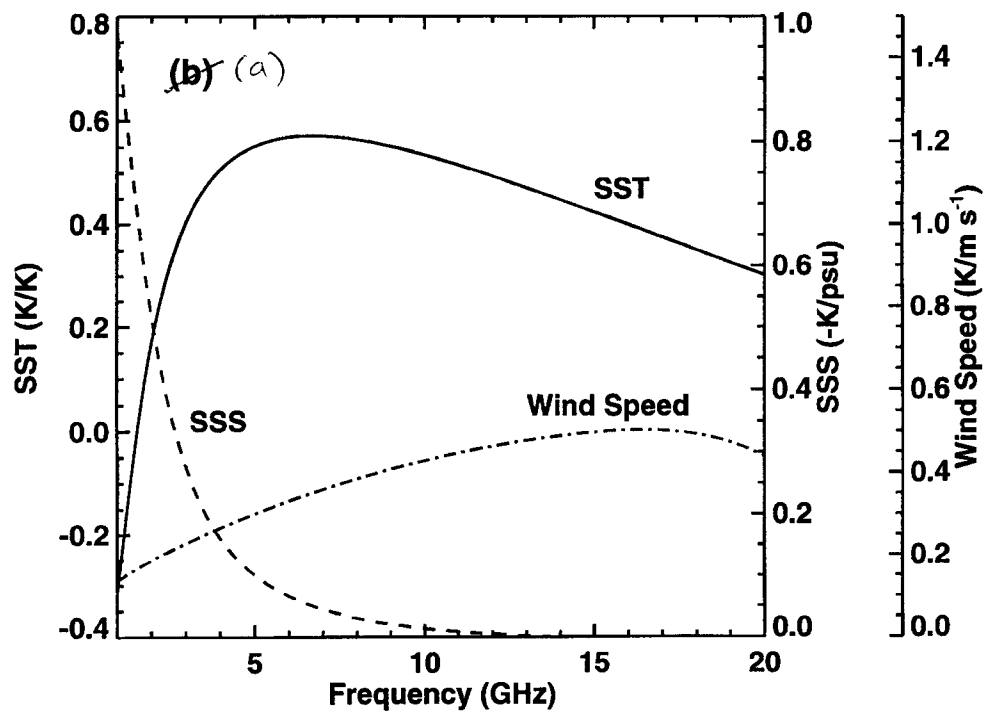


Figure 2(a)

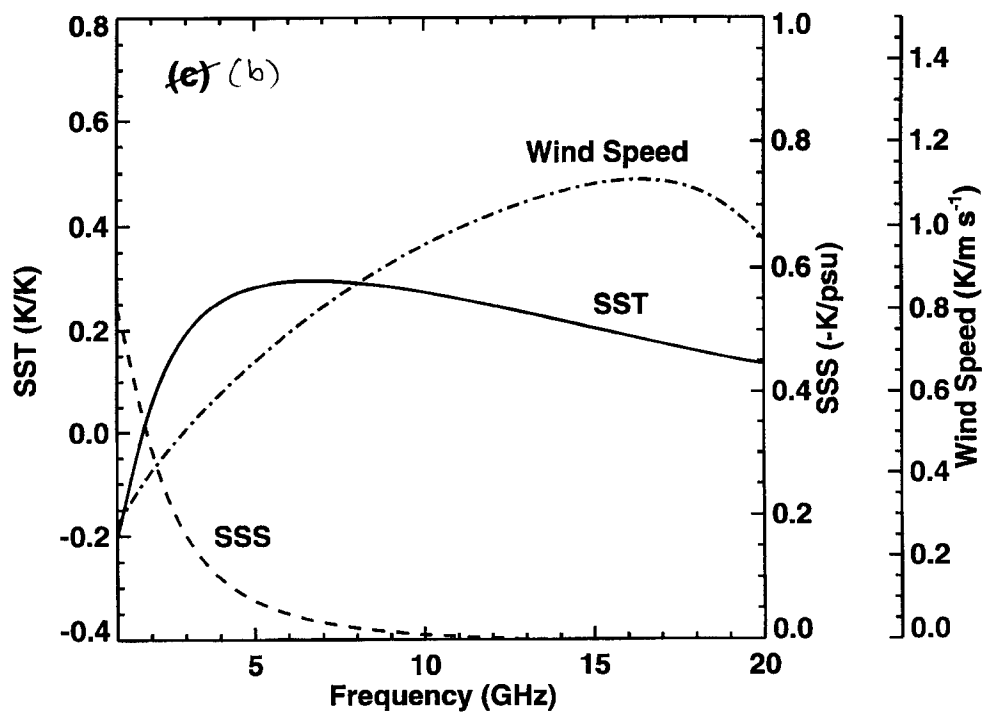


Figure 2(b)

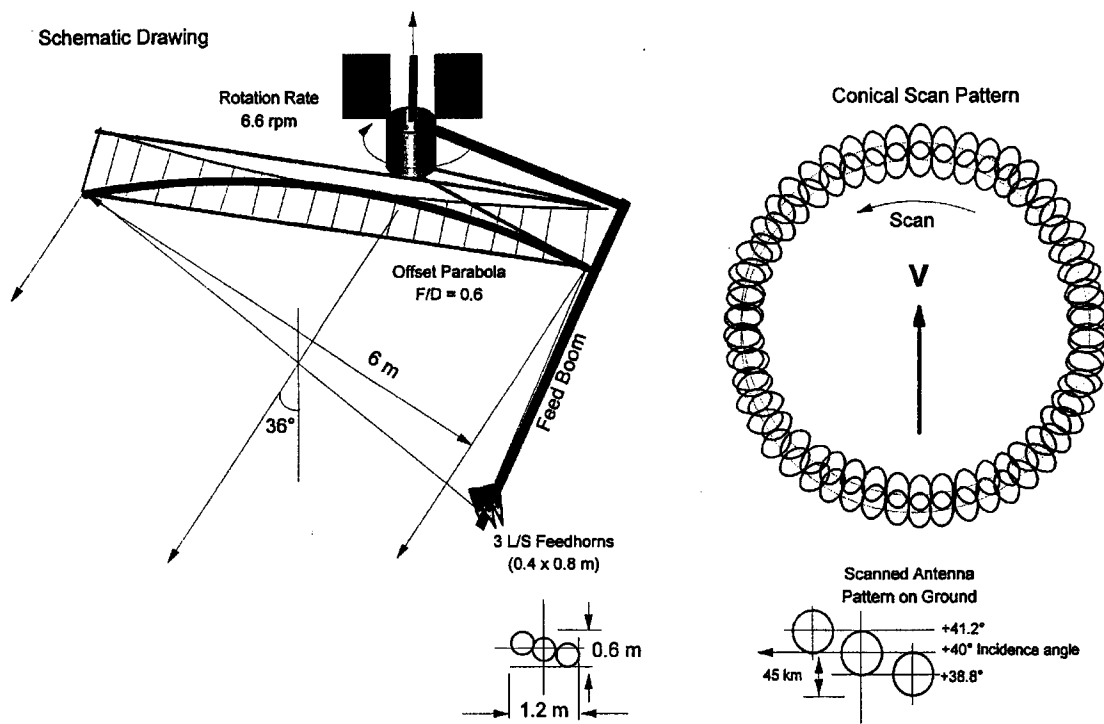
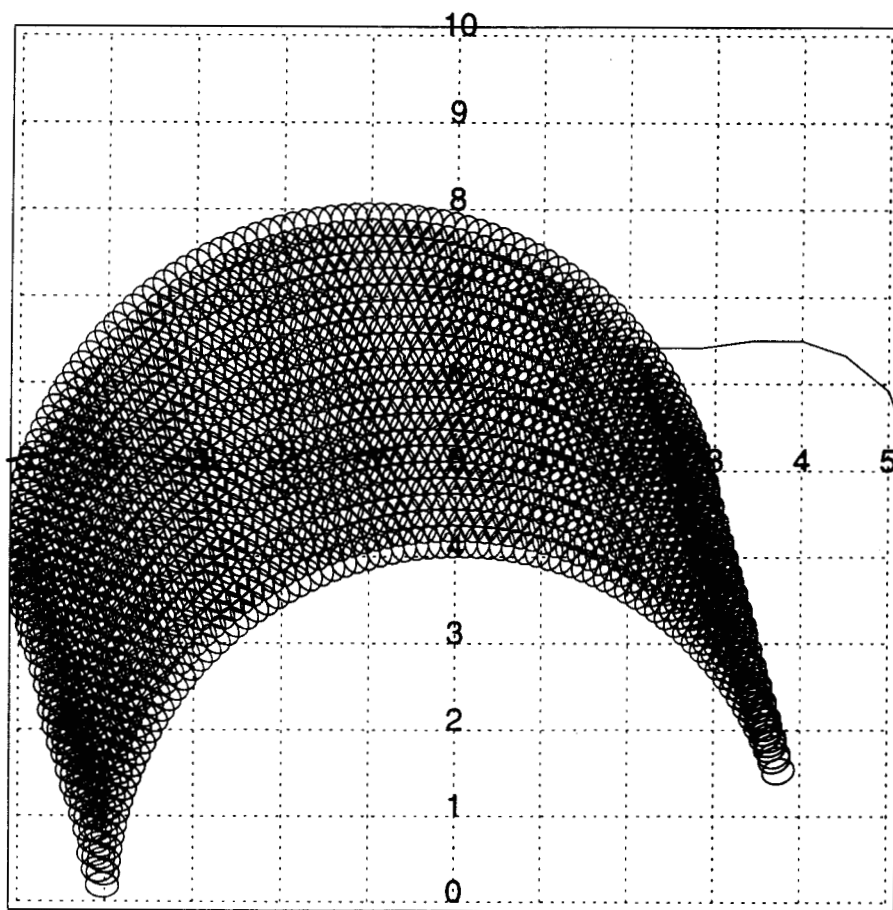


Figure 3

Figure 4



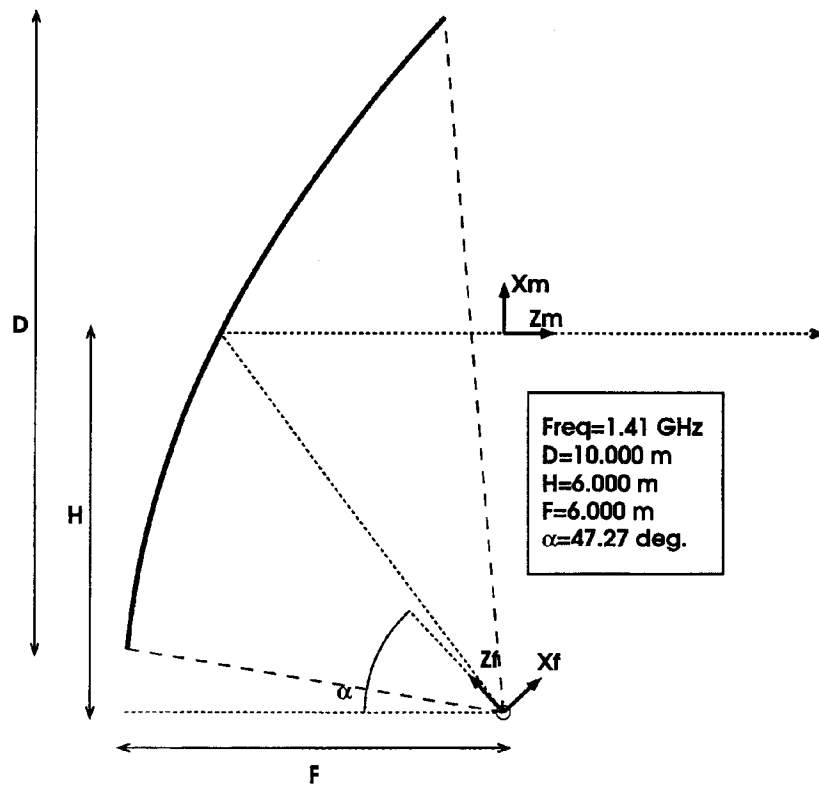


Figure 5

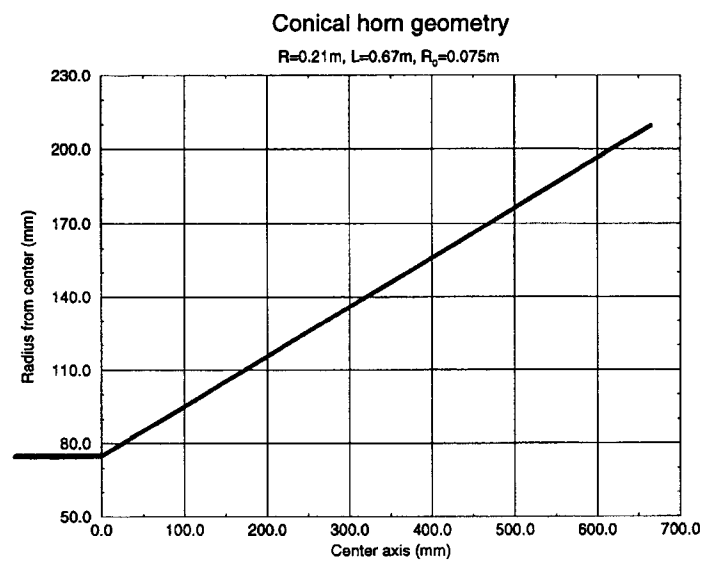


Figure 6

Parabolic Reflector Antenna

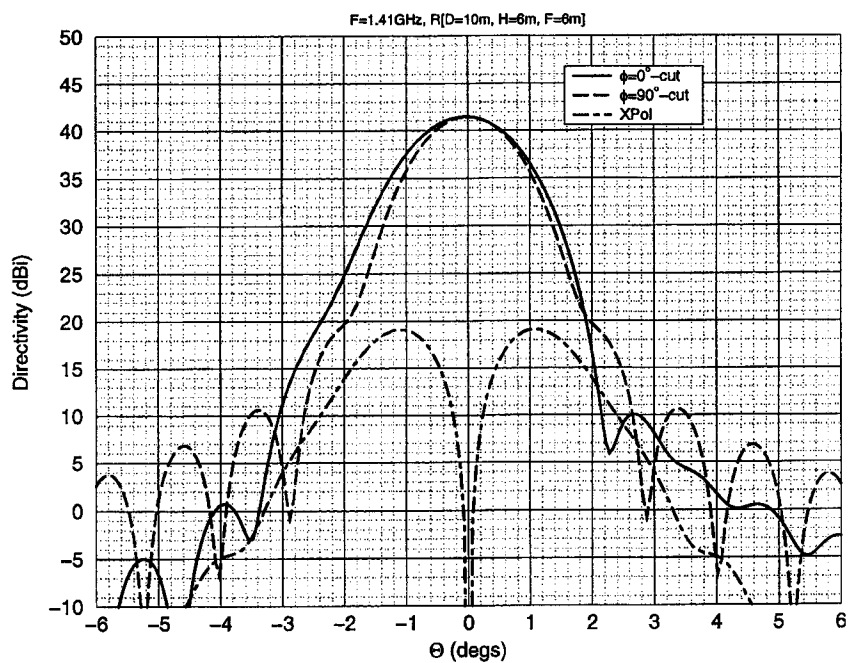


Figure 7(a)

Parabolic Reflector Antenna

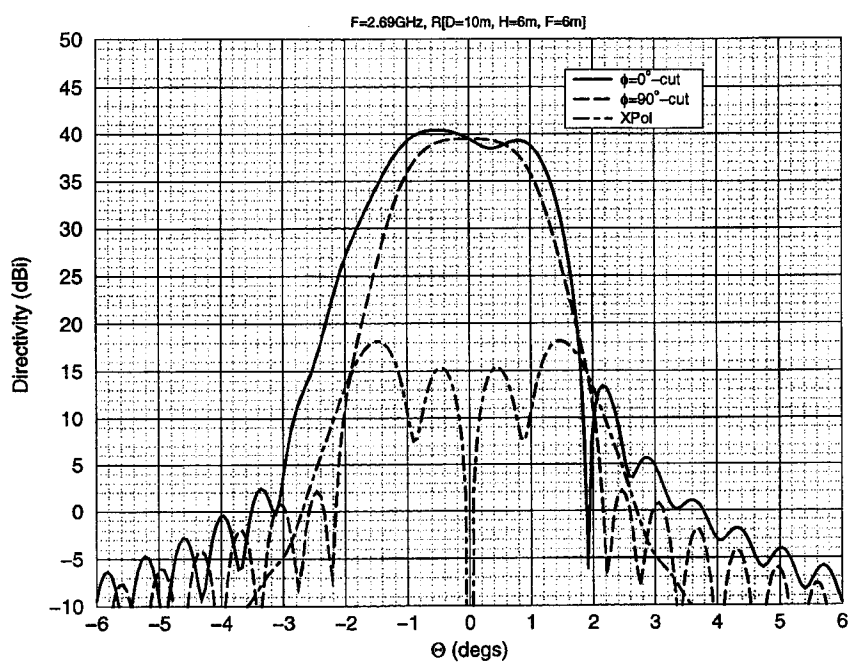
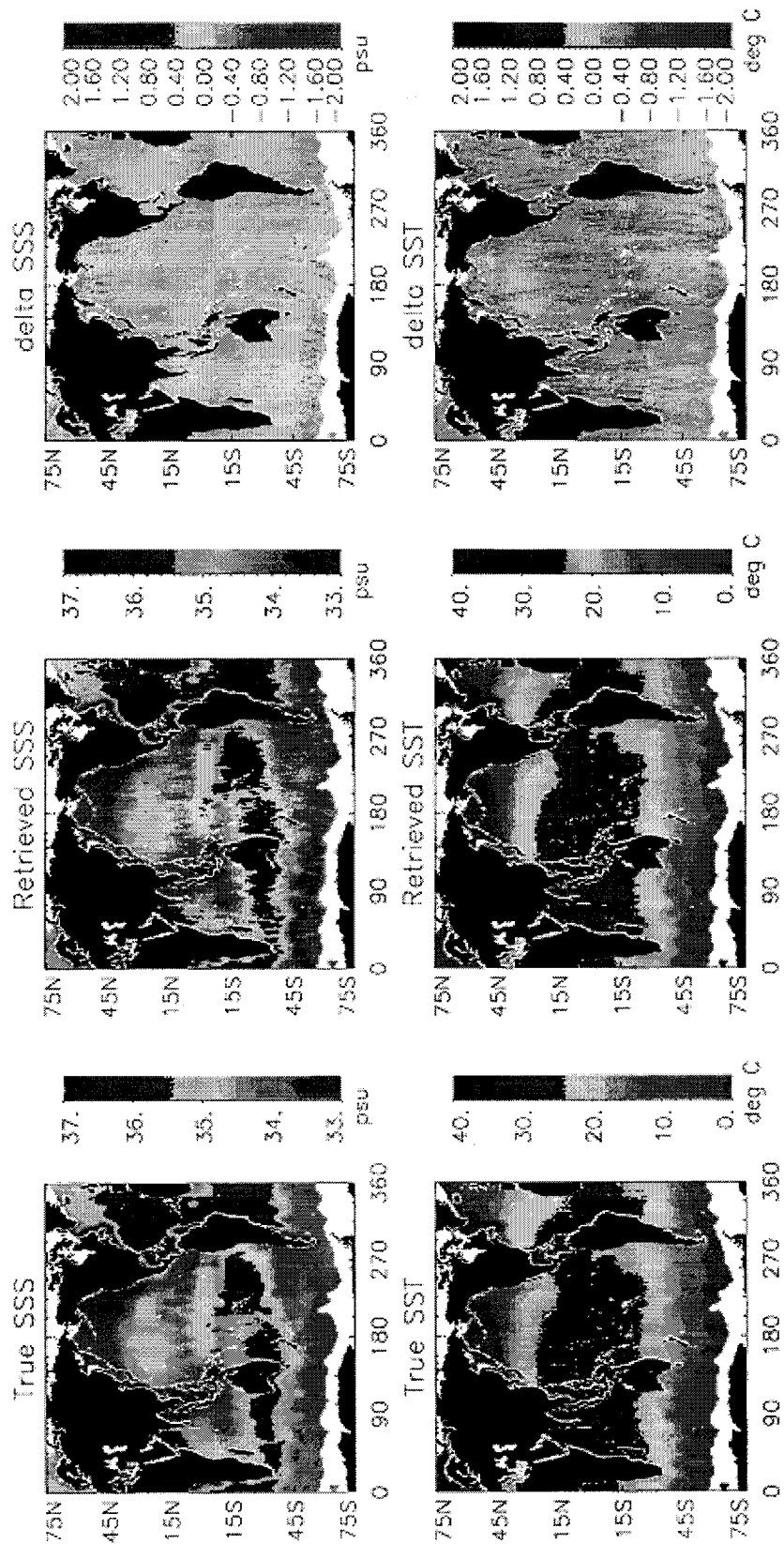


Figure 7(b)

Salinity Retrieval Simulation (7 Days of Data)

L-/S-Band Radiometer And L-Band Radar



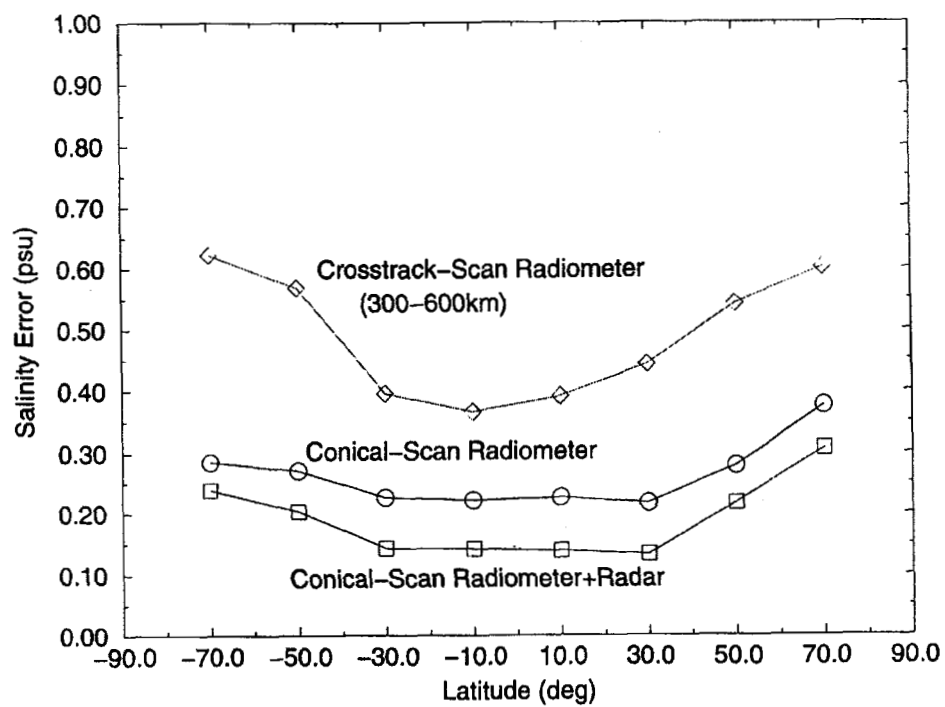


Figure 9